Ballistic impact behaviour of glass fibre reinforced polymer composite with 1D/2D nanomodified epoxy matrices

Nadiim Domun[a], Cihan Kaboglu[b], Keith R. Paton[c], John P. Dear[b], Jun Liu[b], Bamber R.K. Blackman[b], Gholamhossein Liaghat[a], Homayoun Hadavinia[a,*]

[a] Department of Mechanical Engineering, Kingston University London, UK
[b] Department of Mechanical Engineering, Imperial College London, UK
[c] National Physical Laboratory, Hampton Road, Teddington, Middlesex, UK

ABSTRACT

In this paper, experimental studies on the ballistic impact behaviour of nanomodified glass fibre-reinforced polymer (GFRP) are reported. The epoxy matrix of the GFRP was modified by the addition of graphene platelets (GNPs), carbon nanotubes (CNTs), combined hybrid hexagonal boron nitride nanosheets (BNNS)/CNT, and combined boron nitride nanotubes (BNNTs)/GNPs nanoparticles.

Ballistic impact tests were carried out on GFRP laminates at two projectile velocities of $76 \pm 1 \, \mathrm{m\,s^{-1}}$ for full-field deformation measurements and $134.3 \pm 1.7 \, \mathrm{m\,s^{-1}}$ for perforation tests. The behaviour of the plates during impact was recorded using digital image correlation (DIC), in order to monitor strain and out-of-plane deformation in panels with nanoreinforced matrices. Following penetrative impact tests, pulse thermography was used to characterise the delamination of impacted plates. The results of full-field deformation, exit velocity and energy absorption measurements from the ballistic tests show significant improvements in impact resistance for the panels made from nanomodified epoxies relative to laminates with the unmodified epoxy matrix. The highest absolute absorbed energy was observed for the GFRP panels fabricated using the epoxy matrix loaded with BNNT/GNP at 255.7 J, 16.8% higher than the unmodified epoxy matrix.

1. Introduction

Many advanced structures use fibre-reinforced polymer (FRP) composite materials extensively, such as fuselages of aircraft [1] and wind turbine blades [2]. For example 22% of the primary structures in the Airbus A380 are made from GLARE, a laminate consisting of Aluminium/GFRP alternating layers and the Boeing 787 Dreamliner contains about 50% by weight of carbon fibre-reinforced polymer (CFRP) in the fuselage [3], saving 20% of the overall weight compared to aluminium alloys [4]. FRP composites offer higher specific strength, improved corrosion resistance, enhanced damage tolerance and superior fatigue resistance in comparison with traditional metallic alloys such as aluminium and steel. The resulting reduction in aircraft and automobile mass reduces fuel consumption and hence contributes to a reduction in air pollution.

During the service life of aerospace, marine and automotive structures, there is the possibility of foreign objects causing ballistic impact loading from events such as bird strikes, hailstones, shrapnel, runway debris, bullets and blast fragments. As well as the potential of penetration, such impacts can lead to extensive delamination, resulting in degradation of the structural performance [4,5]. The majority of these structures are not designed to act as armour, and due to the possibility that they are likely to be subjected to high-velocity impacts with low-mass fragments, full knowledge of their response to ballistic impact loading and the associated damage mechanisms is required.

During a ballistic impact, a propelling object generally of low mass and high velocity, strikes the structure and causes the propagation of stress waves in the material [6,7]. On impact, instantaneous stresses are generated around the impacted area but these stresses do not immediately transmit to all parts of the structure. In fact, areas of the structure remote from the impacted zone remain undisturbed until the stress waves, which propagate through the body at velocities dependant on the material properties, reach them. Regardless of how the impact load is applied, the propagation of these stress-waves depend only on the target material properties.

Protection against external high velocity projectile impact is one of the critical requirements of FRP composite structures. Such impacts can result in indentation, partial penetration or perforation of the FRP

---

composite target depending on mass, shape, size, and velocity of the projectile and the geometry and mechanical properties of the target FRP structure.

The ballistic impact and energy absorption capacity of glass fibre-reinforced polymer (GFRP) composite structures has been studied by many researchers both experimentally [8–11] and using finite element analysis [12,13]. Experiments were performed to study the effect of thickness and fibre orientation on the ballistic limit and exit velocity. It is reported that the laminates with (0/90) lay-up sequences are most effective in impact resistance and absorbed energy is increased non-linearly with increase in thickness of laminates. Studies carried out on glass fibre–aluminium laminate (GLARE) showed that energy absorption and the ballistic limit of either the Aluminium or glass fibre composite from which it was made has been increased [14,15].

In recent years, the use of one-dimensional (1D) and two-dimensional (2D) nanomaterials as a reinforcing material in a polymer matrix has attracted much research attention with significant improvements in fracture toughness reported [16,17]. Some published works have shown that effective dispersion, as well as improved interfacial properties, were achieved by introducing two-component hybrid 1D/2D nanoadditives to the polymer matrix to generate a synergistic effect [18–20]. For example, Domun et al. [16] studied two hybrid nanoparticles systems; one consisted of functionalized f-MWCNT with hexagonal BNNS and the other was made of plasma-functionalized f-GNP with BNNT to improve the fracture toughness of the resultant epoxy nanocomposites. Hybrid f-MWCNT/BNNS at (0.1:0.1) wt.% loading content resulted in an increase of 71.6% in fracture toughness compared with the unmodified epoxy. For the hybrid f-GNP/BNNT system at (0.25:0.1) wt.% loading, the fracture toughness of the epoxy nanocomposite was increased by 91.9% relative to the unmodified epoxy. The toughening mechanisms were associated with crack bridging, crack pinning and deflection as observed from fractography analysis [21].

Using nanoadditives in the polymer matrix has been shown to improve the ballistic performance of FRP composites. This is evidenced by numerous published works, such as Tehrani et al. [22] and Laurenzi et al. [23], who have shown that the enhancement of the ballistic impact resistance of FRP composites was achieved by adding CNT to the polymer matrix. Rahman et al. [24] experimentally studied the ballistic impact behaviour of E-glass/epoxy modified with MWCNT. They reported an increase in the ballistic limit of around 5% for the composite with the addition of MWCNT. Pandya et al. [25,26] investigated the ballistic impact behaviour of CNT and nanosilica modified resin and GFRP composites. They concluded that the inclusion of nanoparticles in the epoxy matrix improves the ballistic limit, i.e. the velocity required for a projectile to reliably (at least 50% of the time) penetrate the material, and energy absorption, while damage size around the point of impact decreased. Pol et al. [27,28] studied the effect of the loading ratio of nanoclay on the impact behaviour of 2D woven glass/epoxy/nanoclay composite by ballistic impact tests. The composite showed the best ballistic behaviour with the addition of 3 wt% nanoclay at an incident velocity of 134 m s^{-1}.

Avila et al. [29] modified fibre glass/epoxy with nanoclay, graphene and ceramic layers in ballistic tests under incident velocities of 242 m s^{-1} and 355 m s^{-1}. In general, they concluded that nanoclay and graphene sheets improve the ballistic behaviour of the composite and affect the failure mechanism of the composite at the same time. Crack propagation energy is increased by addition of the filler materials, leading to increased interlayer shear failure and delaminations.

The effects of low-dimensional nanoparticles in improving the fracture toughness of bulk epoxy resins have been previously reported [16,30]. In the current work, we extend this study to investigate the ballistic impact performance of GFRP laminates with nanomodified epoxy matrix. Ballistic tests have been carried out, confirming that significant improvements in impact resistance of the composites made with the reinforced matrix have been achieved in the highly dynamic impact tests. Enhancement in ballistic impact resistance of the

nanomodified resin is measured by the exit velocity of the projectile and specific energy absorption (SEA).

2. Materials and methods

2.1. Materials

The resin used in this study was a two-part low viscosity epoxy, Araldite® LY 564 resin and cycloaliphatic polyamine Aradur® 2954 hardener supplied by Huntsman. The normal ratio of resin to hardener of 100:35 by weight was used, giving a gel time of approximately 90 min at 60 °C.

Graphene nanoplatelets were supplied by Haydale Ltd., which had undergone a proprietary plasma process (HDPlas® GNP- O$_2$ -STD, Batch Number: 8039). They were used without further modification. Multi-walled carbon nanotubes (MWCNT) NC3100 were purchased from Nanocyl SA (Sambreville, Belgium) which were produced by catalytic chemical vapour deposition (CVD) process. The average diameter of the MWCNT was given by the supplier as ~9.5 nm with an average length of 1.5 μm and a carbon purity of > 95.0%. The HNO$_3$, methanol and ethanol were of analytical grade and were obtained from Sigma-Aldrich (Poole, UK). Multi-walled boron nitride nanotubes (BNNT) purchased from NAiEEL Technology (Daejeon, South Korea) had an average diameter of 100 nm with length > 1 μm and were used as-received. Hexagonal boron nitride powder (h-BN) was purchased from UK Abrasives, Inc (Northbrook, IL, USA).

The f-MWCNTs used in this study were prepared following a procedure described previously [16]. Briefly, unmodified MWCNTs (0.1 g) were dispersed in 100 ml of HNO$_3$ (70%) in a round-bottom flask (250 mL) equipped with a condenser and refluxed at 135 °C for 24 h. Next, the mixture was diluted in deionised (DI) water (18.2 MΩ cm) and filtered on a Millipore™ Isopore filter membrane (Millipore, Watford, UK). The collected solid was then repeatedly washed with DI water, methanol, and ethanol until a neutral pH was reached, and subsequently dried in vacuum at 40 °C.

Functionalized BNNS was prepared by the heat treatment of hexagonal boron nitride in air. In a typical experimental run, 20 g of h-BN powder was placed in a quartz tube in a tube furnace. The furnace was heated to 1000 °C and held at that temperature for two hours in air, and then the hBN washed with hot water. SEM images of nanoparticles used in this study are shown in Fig. 1 confirming the expected morphology of each filler type.

2.2. Manufacturing nanocomposite laminates

The fibre reinforcement used for this study was purchased from Marinewear Ltd (Eastleigh, UK). Non-crimp glass fibre fabric with a quasi-isotropic sequence [45/90/-45/0] was used to manufacture the specimens for ballistic impact tests.

A hand lay-up process was used to produce the GFRP laminates, followed by vacuum bagging during curing of the epoxy matrix. The nanocomposite-based epoxy was developed using exactly the same procedures as described in Ref. [16]. The filler was dispersed in methanol by sonication and the epoxy was added dropwise. The solvent was extracted by evaporation under vacuum condition. A high-speed mixer was employed to mix the final nanocomposite compound. The resulting four epoxy modified nanofillers used were at 0.25 wt% GNP, 0.1 wt% CNT, 0.1:0.1 wt% of (CNT:BNNS) and 0.25:0.1 wt% of (GNP:BNNT) in addition to a control sample of neat epoxy.

3. Ballistic impact tests

3.1. Ballistic test set-up

High-velocity impact tests were conducted using a helium gas gun with a 4-L pressure vessel, connected to a 3 m long barrel by a fast
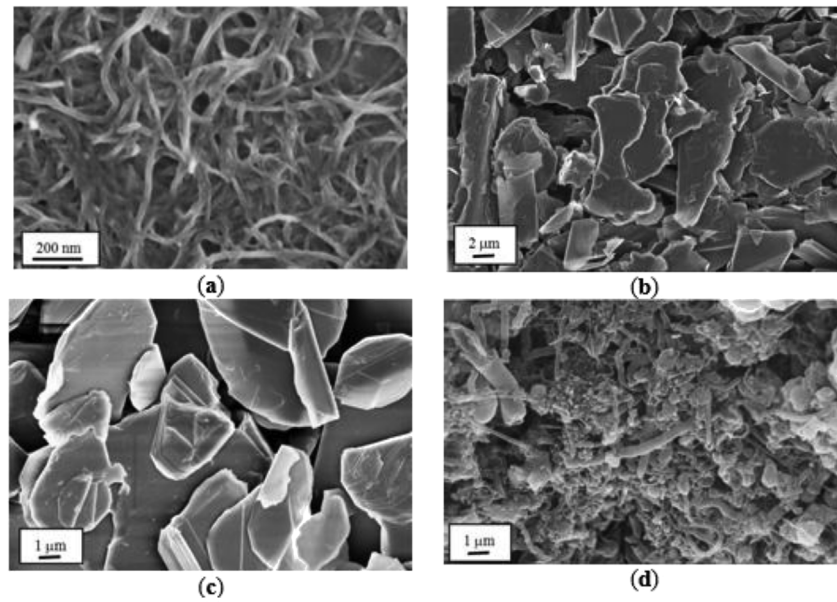
Fig. 1. SEM images of nanoparticles used in hybrid nanocomposites: (a) MWCNT; (b) f-GNP; (c) BNNS; (d) BNNTs [16].
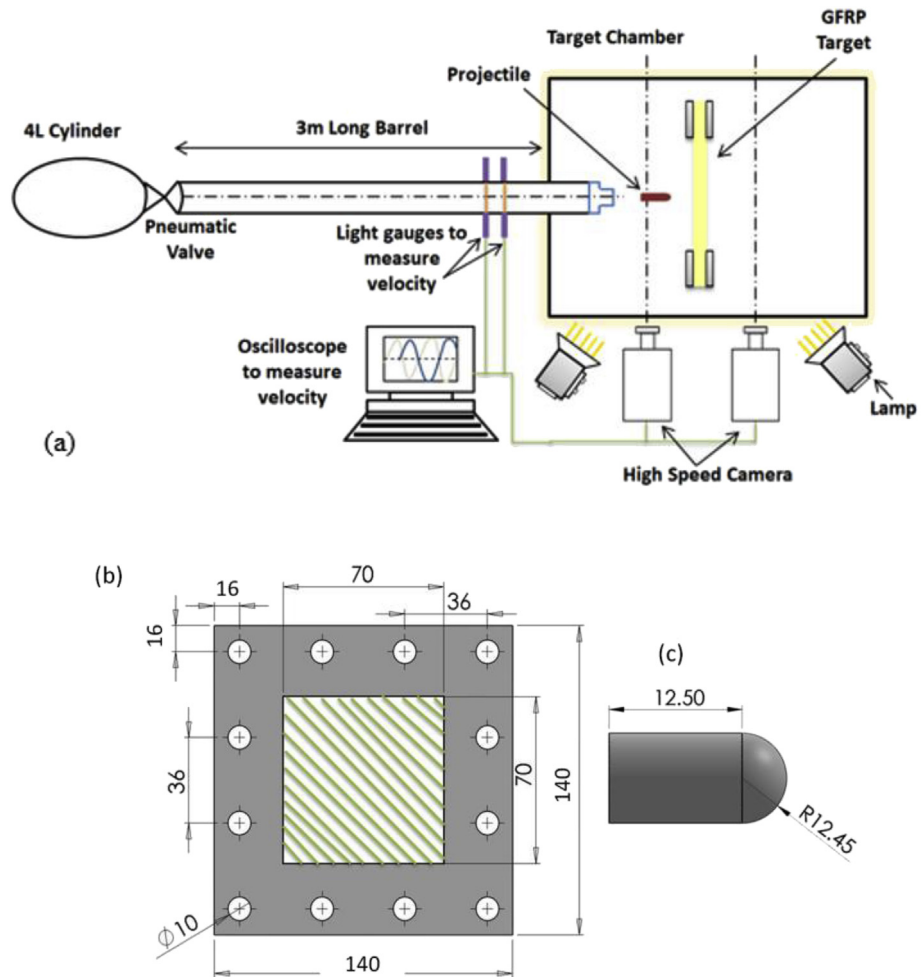

Fig. 2. (a) Schematic of gas gun for high velocity impact test, (b) Schematic of a target GFRP specimen in the clamp for ballistic test, (c) Technical drawings of projectile.

acting pneumatic valve. Two types of ballistic test set-up were employed: a high-energy test to investigate penetrative impact; and a lower energy test, measuring out-of-plane deformation and in-plane strain. In the high-energy tests, shown in Fig. 2a, the pressure of the vessel was set to 4 bar and the GFRP plates were impacted by a projectile at an average velocity of $134.3 \pm 1.7 \, \mathrm{m\,s^{-1}}$. The aim was to investigate the exit velocity and energy absorption, as well as the post-perforation damage. All GFRP ballistic specimens had 24 layers with a quasi-isotropic sequence of $(+45/90/-45/0)_3/(0/+45/90/-45)_3$ with a nominal thickness of $3.8 \pm 0.2 \, \mathrm{mm}$. For both series of tests, the GFRP plates had holes drilled around the periphery with a diameter of 8 mm. This allowed clamping of the specimens around the edges using twelve M8 bolts. A schematic drawing of the specimen and the clamp are presented in Fig. 2c. The opening of the clamps is 70 mm × 70 mm as shown in Fig. 2c.

The projectiles were cylindrical with a hemispherical nose, with a diameter of $24.9 \pm 0.1 \, \mathrm{mm}$ (Fig. 2b). They were made from aluminium alloy with HV5 hardness of 192 ± 5 and a mass of $m_p = 28.5 \pm 0.1$ g. No plastic deformation was observed in the projectile after impacting the target. The velocity of the projectile was measured using a pair of IR sensors located at the end of the barrel. Two high-speed cameras (Phantom Miro M/R/LC310) were located perpendicular to the travel direction of the projectile (Fig. 2a). One of the cameras was employed to measure the inlet velocity of the projectile before impact (the velocity measurements were compared against those measured by the two IR sensors and confirmed to be accurate). The second camera was used to measure the exit velocity of the projectile after perforations of the plates were attained. A transparent safety chamber, mainly made of thick polycarbonate panels, was used to confine the end of the barrel as well as the target area.

A second series of lower energy impact tests were conducted according to the set-up reported by Kaboglu et al. [31]. The ARAMIS 3D Digital Image Correlation system was used to obtain the full-field deformation map and major in-plane strains of GFRP composite plates with various matrices for velocities below the ballistic limit [32]. In these tests as shown in Fig. 3a, the two high speed cameras were moved to the back side of the target separated by a distance of 410 mm and 925 mm from the centre point of the target and the angle between the two cameras was 25°. The back surfaces of the specimens were illuminated by two halogen lamps to avoid any shadows from nearby objects, which were turned on a few seconds before the start of firing the projectile. The cameras were used to record at a rate of 39,000 frames per second. A pair of identical Nikon lenses with a fixed focal length of 50 mm was used for both cameras. These cameras were triggered simultaneously by the signal generated from the IR sensors at the beginning of the tests. One side of each specimen was painted with matt white spray paint to avoid getting reflection of light on the specimen and to conceal any imperfections on its surface and then speckled by hand using a matt black marker with the size of the black speckles around 1.5–2.0 mm. The high contrast, randomly generated unique speckle patterns on each facet were tracked by the ARAMIS software, and the deformation field was calculated from the sequence of images from the two high-speed cameras and strain was determined from the calculated displacement.

The three critical length scales associated with DIC are speckle size, facet size, and facet step. Speckle pattern and size chosen prior to a ballistic test are based upon deformation, features of interest, field-of-view, resolution, and structure length scale [33]. Facet size is the correlation window, i.e. a relatively small aperture that comprises multiple speckles used for intensity pattern matching. The last length scale facet step is defined as the facet overlap length usually about 2 pixels. The latter two parameters – facet size and facet step – are chosen during the post-processing of DIC data. The size of the facets and the level of overlap are very important for measuring the strain. In this research, the area of the specimen is 70 mm × 70 mm and the image resolution is 256 × 256 pixels. As a result, each pixel is 0.273 mm and the area of each pixel is $0.07477 \, \mathrm{mm^2}$. The recommended minimum speckle size is 5 pixels resulting in speckle area of $0.374 \, \mathrm{mm^2}$ and diameter of 0.7 mm.
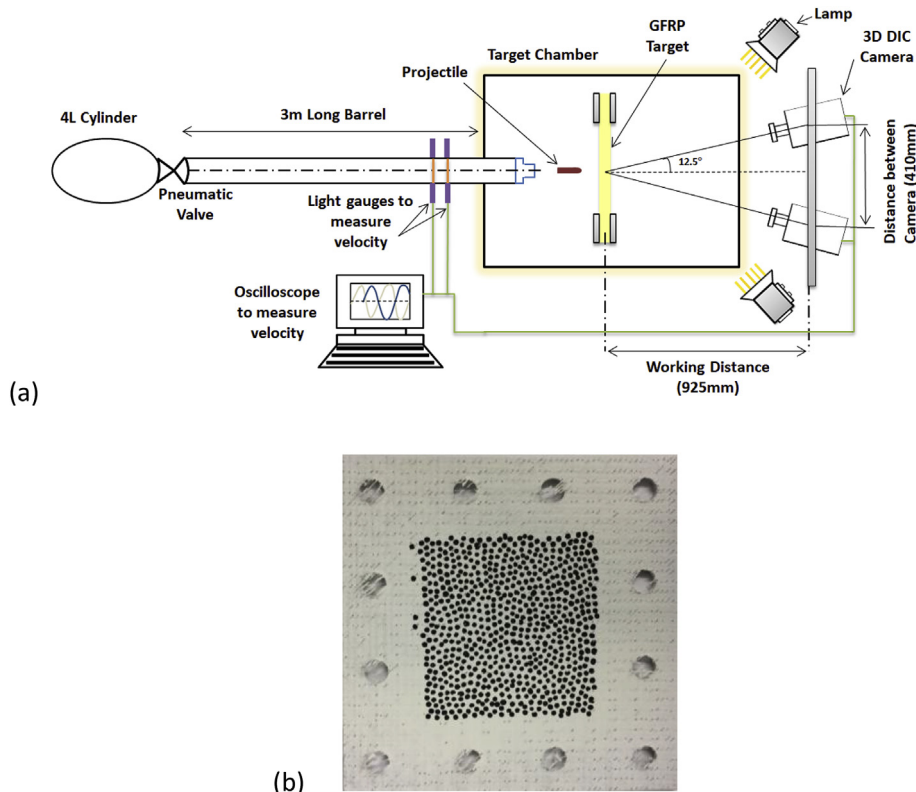

(a)

(b)

Fig. 3. (a) Schematic of gas gun for high velocity impact test with 3D DIC, (b) a GFRP specimen with a speckle pattern before ballistic test.

This minimum speckle size is the smallest readable size by the software. Anything larger is acceptable. In this research, the speckle has diameter of ~1.5 mm resulting in approximately 1.77 mm^2 area, roughly 4.7 times the minimum acceptable size. The accuracy of strain is ca. 0.05% under best condition. Black and white paints were chosen to maximise contrast. An example of a specimen with a typical speckle pattern is shown in Fig. 3b.

The projectiles used for these experiments were the same as in the first series of ballistic tests. In this series of tests, the pressure of the vessel was set to 1.5 bar and the GFRP plates were impacted by a projectile at an incident velocity of $76 \pm 1\,\mathrm{m\,s^{-1}}$ (equivalent to 273.6 km/h) which resulted in all projectiles rebounding back. This speed is the upper limit in automotive accidents. The projectiles were retrieved after the impact tests, and after inspection, no plastic deformation of the projectile following impact was observed and almost all the impact energy was absorbed by the target plates.

3.2. Ballistic test results and discussion

3.2.1. Results of perforated ballistic tests

In this series of tests, all specimens were perforated under ballistic impact with an average velocity of $134.3 \pm 1.7\,\mathrm{m\,s^{-1}}$ (equivalent to 482.4 km/h). Commercial aircraft approaching landing has speed around this range and bird strike is likely impact event during approach to landing. Following impact testing, the panels were visually inspected for damage. There was noticeably more damage on the rear face of the GFRP with (EP + BNNS + CNT) matrix compared to the other matrices, which showed little clear difference between them. Across all the specimens, similar behaviour in the crack propagation was observed along the fibre in $\pm 45°$ direction as seen from the rear surface of impacted specimens.

The exit velocity (V_e) of the projectiles in this series of tests together with the percentage in reduction of incident velocity (V_i) is shown in Fig. 4a. The results show that all nanomodified epoxy matrices have reduced the exit velocity relative to the neat epoxy. The GFRP with neat epoxy experienced a reduction in the exit velocity by 67%, from $131.6\,\mathrm{m\,s^{-1}}$ to $43.4\,\mathrm{m\,s^{-1}}$. The highest reduction in the exit velocity was achieved by GFRP with (EP + BNNT + GNP) modified matrix. This matrix reduced the incident velocity by 89.1% from $135\,\mathrm{m\,s^{-1}}$ to $14.7\,\mathrm{m\,s^{-1}}$. Therefore, GFRP with (EP + BNNT + GNP) matrix contributed an additional 22.1% to the reduction of exit velocity on top of the reduction in exit velocity in GFRP with unmodified epoxy matrix.

The absorbed energy (E) and specific energy absorption (SEA) were calculated from

$$E = \frac{1}{2}m_p(V_i^2 - V_e^2) \tag{1}$$

$$SEA = \frac{E}{m_{GFRP}} \tag{2}$$

The highest absolute absorbed energy was observed for the instance of the GFRP with (EP + BNNT + GNP) matrix at 255.7 J, 16.8% higher than the unmodified epoxy matrix. However, the (EP + BNNT + GNP) specimen was heavier than the neat epoxy specimen. The mass of glass fabric (m_{GFRP}) in both specimens was the same and the difference is due to the surplus of matrix (see Table 1). The (EP + BNNT + GNP) specimen had 8.7% more resin than the neat epoxy specimen. This effect can be compensated for by comparing specific energy absorption (SEA) for all specimens in Table 1 and Fig. 4b. It is evident that even with this adjustment, all nanomodified GFRPs have higher SEA than unmodified GFRP, but the best performing matrix based on the SEA criteria is (EP + BNNS + CNT) with 16.3% higher SEA than the unmodified epoxy matrix. Overall, the average increase in SEA for nanomodified epoxy GFRPs relative to unmodified epoxy GFRP is 11.4%. It is evident that the change in the fibre volume fraction had a direct effect on the exit velocity. The (EP + BNNT + GNP) specimen had 8.7% more resin relative to the unmodified epoxy specimen. It is reported that stick-slip frictional motion between the nanoparticles and the epoxy resin is the source of interface damping [34] and debonding slippage occurring between nanoparticles and the matrix under external force, resulting in interface friction, which in turn led to energy dissipation [35]. The reduction in exit velocity seen for (EP + BNNT + GNP) specimen is partly due to the excess resin, as polymers have a damping effect on the projectile.

3.2.2. Unperforated ballistic tests

Fig. 5 shows the variations of major strains along the centre line (CL) at the end of loading (when projectile has come to a stop) and at the end of the unloading (when the projectile loses contact with the panel) for all specimens with different matrices. The duration of the impact for all specimens was identical. It is noticeable that in the loading cycle the epoxy behaved as the most compliant laminate with the highest strains. At the end of unloading, the average residual strain in the neat epoxy specimen is also the highest, showing the most permanent damage occurring within this specimen. The minimum residual strain at the end of the test is attributed to the GFRP with (EP + BNNT + GNP) matrix, demonstrated by the minimum permanent damage.

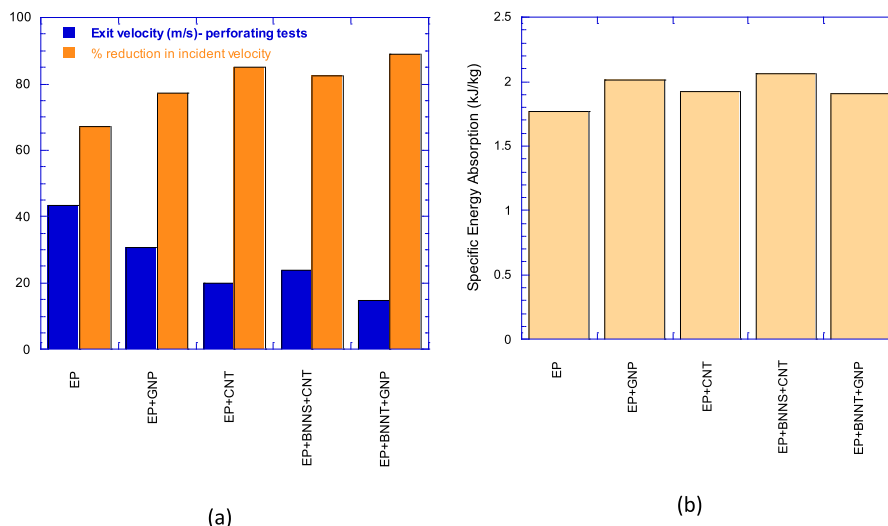In Fig. 6a, the out-of-plane displacement maps of the five different

Fig. 4. Effect of nanomaterials on (a) reduction of exit velocity, and (b) specific energy absorption by GFRP plates in perforating ballistic tests.

Table 1
Summary of perforated ballistic tests results.

Matrix	m_{GFRP} (g)	m_p (g)	V_i (m s^{-1})	V_e (m s^{-1})	% of decrease in V_e	Absorbed energy (J)	SEA (kJ kg^{-1})	% change of SEA relative to neat epoxy
Neat epoxy	123.4	28.4	131.6	43.6	67.0	218.9	1.77	–
EP + GNP	121.8	28.4	135	30.6	77.3	245.5	2.02	+13.6
EP + CNT	132.2	28.5	135	20.1	85.1	253.9	1.92	+8.3
EP + BNNS + CNT	121.5	28.4	135	23.9	82.3	250.7	2.06	+16.3
EP + BNNT + GNP	134.1	28.4	135	14.7	89.1	255.7	1.91	+7.5

specimens during loading and unloading are compared. The duration of the impact for all specimens is the same. However, the maximum out-of-plane displacement areas (shown in red) are different and it is at minimum for specimen with (EP + BNNT + GNP) matrix. The map of major strain distribution during 0.4 ms impact duration is shown Fig. 6b.

Fig. 7 illustrate the post-impacted images of the front and rear surfaces of the GFRP plates for neat epoxy and various nanocomposite matrices. The damage in laminate with (EP + BNNS + CNT) matrix is noticeably the highest and for (EP + GNP), (EP + CNT) and (EP + BNNT + GNP) matrices are relatively lower. The main energy-dissipation mechanisms observed during ballistic impact were: (i) lo-calised fibres tearing along the projectile path due to the out-of-plane shear stresses induced by the projectile, (ii) propagation of interply delamination cracks across the plate from the impacted region (see Fig. 8), (iii) spread of matrix crushing and cracking over a larger area along the projectile path, and (iv) tensile fibre failure at the back layers.

4. Post-ballistic impact damage assessment using pulse infrared thermography

Among various non-destructive testing (NDT) techniques, active thermography techniques and specifically pulsed infrared thermography (PT) has shown great potential. This technique has a fast inspection rate capability. The system is contactless, has high spatial resolution and sensitivity, with internal defect detectability using heat conduction [36].

In this work, the extent of the damage in the GFRP specimens after post-ballistic tests is examined by flash-pulse infrared thermography. The flash thermography system used in this project was a Phoenix Medium Wavelength Infrared (MWIR) camera (FLIR systems), recording the IR emissions from the surface of the specimen at 50 Hz frame rate with a Thermal wave commercial image processing software package called MOSAIQ® [37]. A Xenon flash tube lamp with energy output of 2 kJ were used to generate pulsed thermal waves with total pulse duration lasting 30 ms. When this pulsed thermal energy is applied, a thin layer of material on the surface is heated by a few degrees

centigrade. The surface temperature decays as heat is transferred by conduction through the specimen [38,39]. The presence of any discontinuities such as delaminations in the laminate hinders the heat transfer locally. As a result, the surface cooling rate adjacent to the defects is reduced and temperature above discontinuities remains higher than the undamaged areas. The IR camera captures the surface temperature evolution during the entire thermal transient period. The contrast in surface temperature distribution above the defects in comparison with the surface temperature over undamaged areas is used to determine the location and the size of defects such as delaminations. In these series of tests, the lamps and the IR camera were located on the same side of the specimen. The MOSAIQ® software is used to control the camera and flash unit to acquire a short video clip around 2 min long. From the video clips, the location, shape and size of the defect can be measured from the temperature distribution on the surface of the inspected structure. By monitoring changes as a function of time, the depth of defects can also be inferred, with deeper defects observed later, and with a reduced contrast. The elapsed time t is approximately a function of the square of the depth z and the loss of contrast c is proportional to the inverse of the cube of the depth z [40], i.e. $t = z^2/\pi\alpha$ and $c \approx 1/z^3$ where $\alpha = k/\rho c$ is thermal diffusivity of the material, ρ the density of the material, c heat capacity and k thermal conductivity [40,41].

4.1. Test results

The PT images of the first derivatives [42] of heat amplitude with respect to time from the post-ballistic tests with projectile penetration are shown in Figs. 8 and 9. The plane slice images of the raw, the first and second logarithmic derivatives at time 2.29 s shown in Fig. 8 demonstrate that the raw data images do not accurately identify the damage areas.

Fig. 9 shows the first logarithmic derivatives at time 1.02 s, 4.02 s and 7.02 s after the flash showing the delaminated areas were spread from the point of impact. The thermal diffusivity of GFRP is about $\alpha \approx 0.177$ mm^2 s^{-1} [43]. Therefore, the images' time are equivalent to looking at the depths close to the front, mid-plane and back surface of
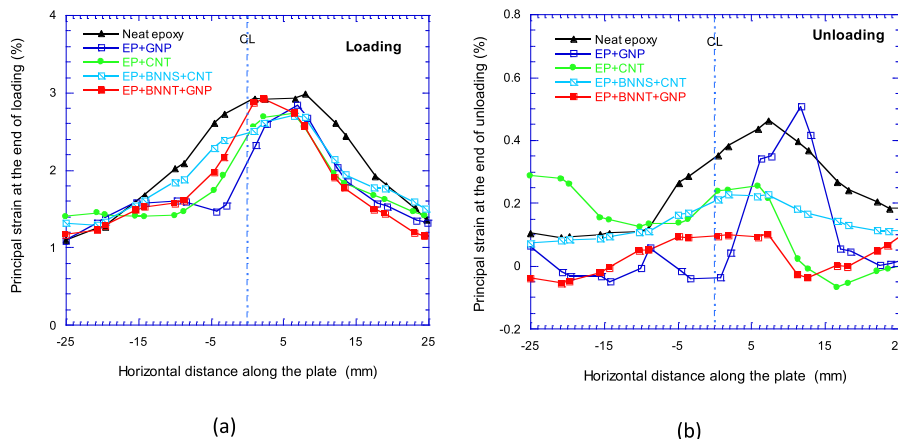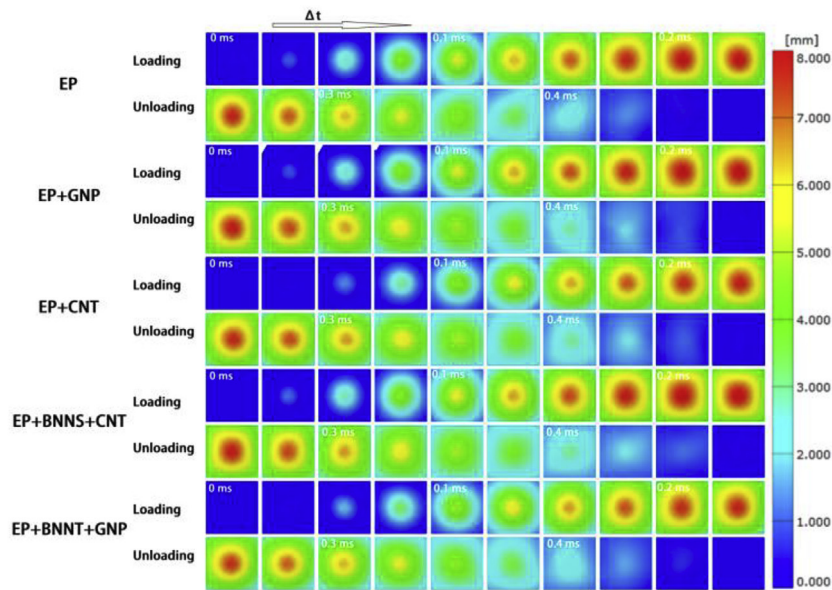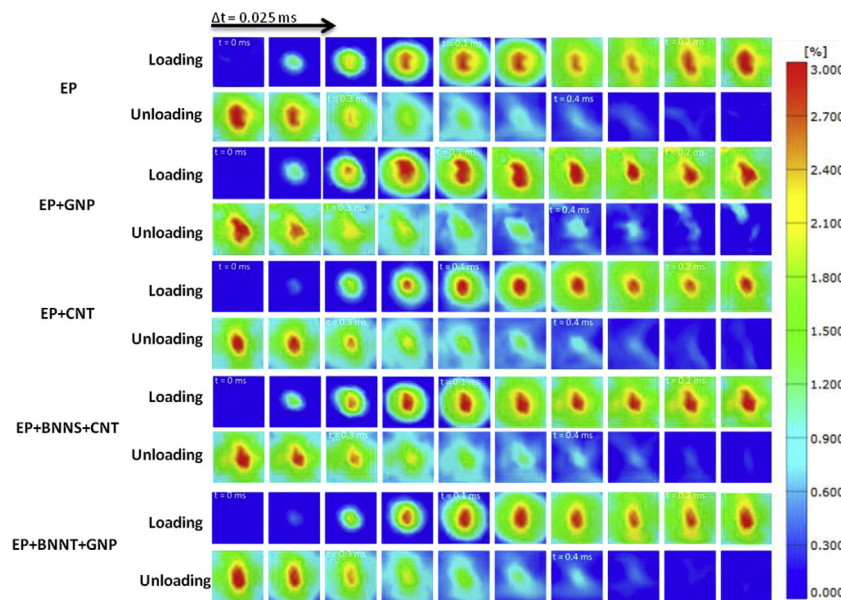

Fig. 5. Principal strain at the end of (a) loading and (b) unloading for all specimens.

(a)

(b)

Fig. 6. DIC full field images of (a) out-of-plane deformation and (b) major strain of GFRP laminated plates during ballistic impact with different epoxy nano-composites under incident velocity of $76 \pm 1 \, \mathrm{m\,s^{-1}}$ when projectile rebounded.

the plates, which have an average thickness of 3.8 ± 0.2 mm. Note however that information from other depths will also be visible in a given frame.

The PT images reveal that the ballistic impact damages are localised around the point of the projectile impact. Visual inspection revealed that there was no evidence of damage on the surface of the laminates except at the projectile impact area and its proximity. All delamination can be observed from the raw thermal images as 'hot spots', but the thermal contrast of smaller or deeper delaminations is very weak in the raw images. The contrast intensity of the delaminations in the first derivatives images is very good, and they show the extent of delamination. The first derivatives are at the peak in part of delamination area,

while the peaks for other shallower delamination occurred at shallower depths (or earlier times).

As shown in Table 1 the highest energy absorption occurred in GFRP with (EP + BNNT + GNP) matrix. This is consistent with the PT images for this GFRP in Fig. 9e showing the highest delamination area in many layers. The minimum damage occurred in neat epoxy GFRP (see Fig. 9a), the projectile entered and left the specimen with minimum energy absorption by the laminate. The extents of the damage shown in Fig. 9 are matching the energy absorption value reported in Table 1 for all types of laminates.
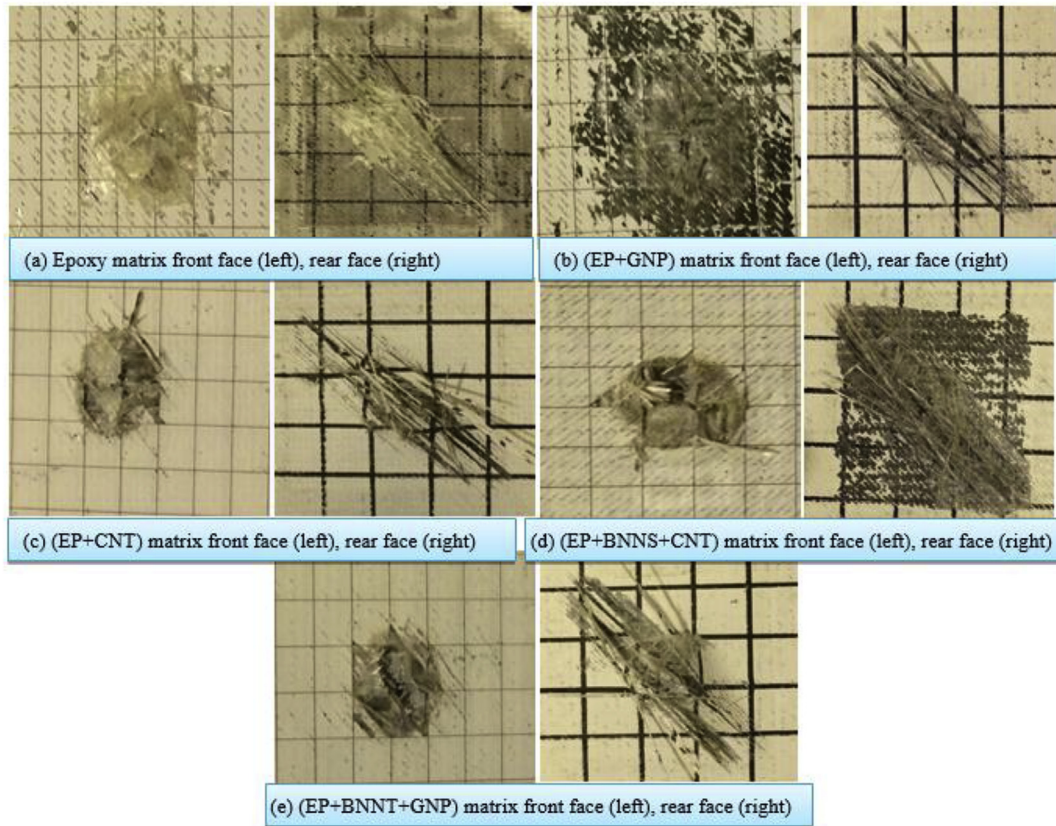
Fig. 7. Images of front and rear faces of impacted GFRP laminates with (a) neat epoxy, (b) EP + GNP, (c) EP + CNT, (d) EP + BNNS + CNT and (e) EP + BNNT + GNP matrices.

5. Conclusions

In the present work, the effect of the modification of GFRP with additive nanoparticles to the epoxy matrix undergoing ballistic impact has been investigated. GNP, CNT, hybrid BNNS + CNT and hybrid BNNT + GNP are used to modify the epoxy matrix.

The ballistic impact tests at two projectile velocities were carried out on the GFRP made from non-crimp quasi-isotropic lay-up of [(45/90/-45/0)$_3$/(0/45/90/-45)$_3$] with different types of resins. At a projectile velocity of 76 $\pm$ 1 m s^{-1} the full-field deformation and major strain are measured without introducing any visible impact damage using DIC system. At a projectile velocity of 134.3 $\pm$ 1.7 m s^{-1} all GFRP laminated specimens were perforated.

The ballistic tests results showed that different nanoparticles within the matrix have an effect on the impact behaviour and damage mechanisms of the GFRP composites. All nanomodified epoxy GFRPs recorded exit velocities lower than neat epoxy GFRP at an incident velocity of 134.3 $\pm$ 1.7 m s^{-1}. The neat epoxy GFRP specimen reduced the exit velocity by 67%, from 131.6 m s^{-1} to 43.4 m s^{-1}. The highest reduction in exit velocity was achieved in the instance of the GFRP with

(EP + BNNT + GNP) modified matrix. This matrix reduced the incident velocity by 89.1%, an additional 18.1% reduction of exit velocity on top of the reduction in exit velocity with the neat epoxy GFRP. Overall, the average increase in specific energy absorption (SEA) achieved for nanomodified epoxies GFRPs relative to the neat epoxy GFRP was 11.4%.

Non-destructive flash-pulsed thermography was employed for post-impact analysis. The images from this method showed that the damage was localised and limited to areas around the impacted point with internal delaminations. To conclude, the incorporation of the various nanoparticles into the epoxy system resulted in a reduction in the exit velocities as well as providing further enhancement in the energy absorption.
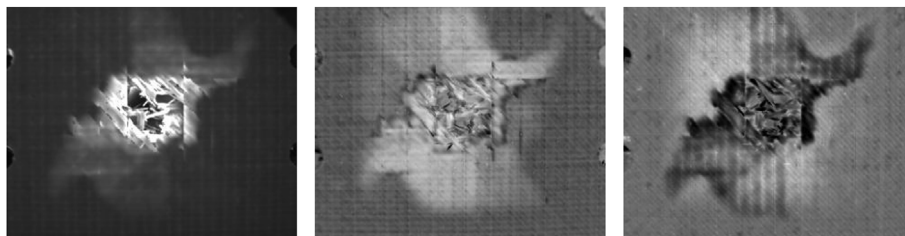
Fig. 8. Raw (left), 1st (centre) and 2nd time differential (right) images of perforated GFRP plates obtained 2.29 s after the flash on GFRP plates with (EP + BNNT + GNP) matrices.
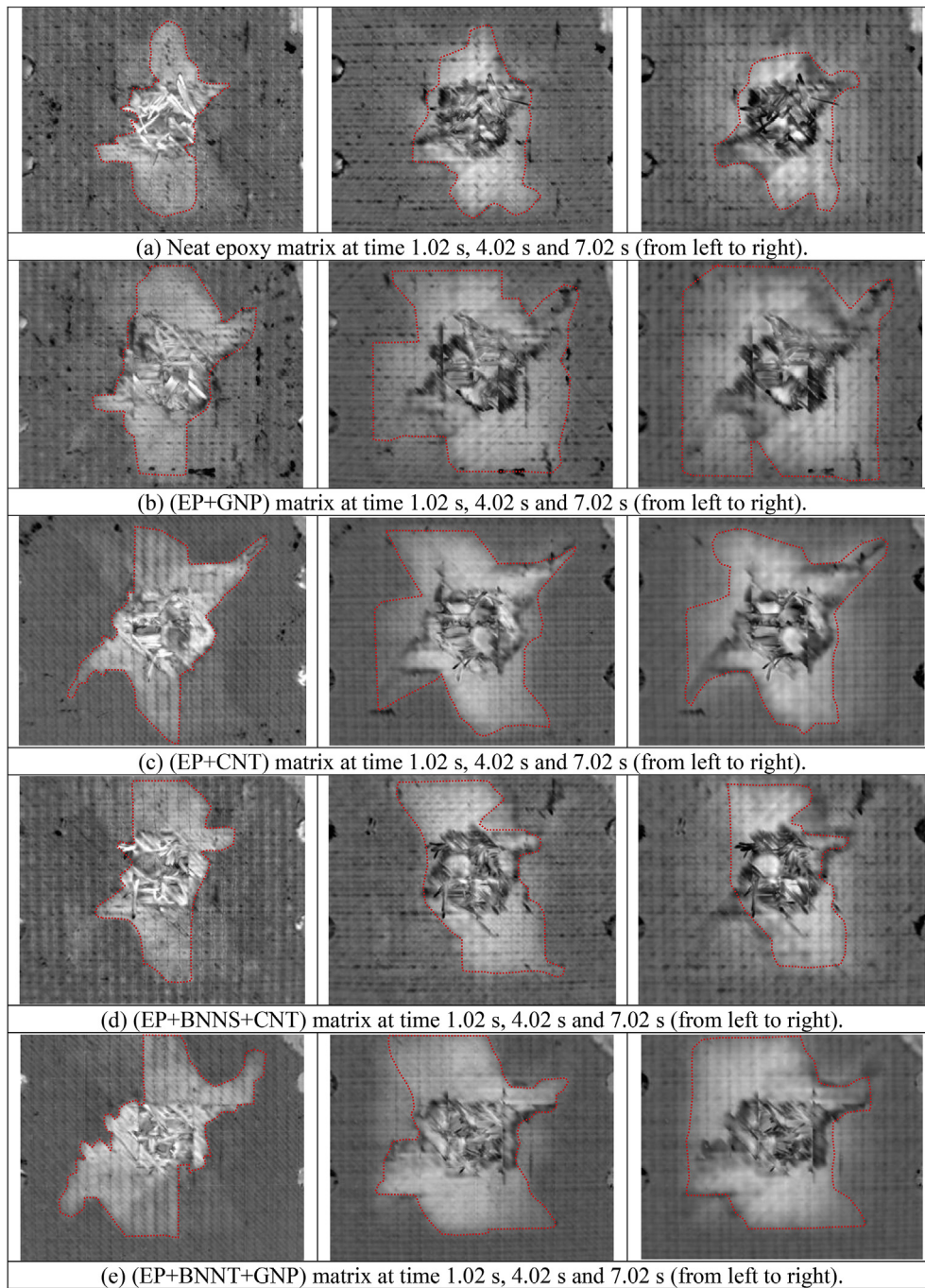
(a) Neat epoxy matrix at time 1.02 s, 4.02 s and 7.02 s (from left to right).

(b) (EP+GNP) matrix at time 1.02 s, 4.02 s and 7.02 s (from left to right).

(c) (EP+CNT) matrix at time 1.02 s, 4.02 s and 7.02 s (from left to right).

(d) (EP+BNNS+CNT) matrix at time 1.02 s, 4.02 s and 7.02 s (from left to right).

(e) (EP+BNNT+GNP) matrix at time 1.02 s, 4.02 s and 7.02 s (from left to right).

Fig. 9. 1st time differential PT images of perforated plates obtained at certain times after the flash on GFRP plates with (a) EP, (b) (EP + GNP), (c) (EP + CNT), (d) (EP + BNNS + CNT) and (e) (EP + BNNT + GNP) matrices impacted with a projectile at 134.3 $\pm$ 1.7 m s^{-1}. The areas identified with damage or delamination are outlined in red to aid the eye. (For interpretation of the references to colour in this figure legend, the reader is referred to the Web version of this article.)

References

[1] Balcıa O, Çobanb O, Borab MÖ, Akagündüzc E, Yalçin EB. Experimental investigation of single and repeated impacts for repaired honeycomb sandwich structures. Mater Sci Eng 2017;682:23–30.

[2] Cai X, Pan P, Zhu J, Gu R. The analysis of the aerodynamic character and structural response of large-scale wind turbine blades. Energies 2013;6(7):3134–48.

[3] Brosius D. "Boeing 787 update", high-performance composites. 2007http://www.compositesworld.com/articles/boeing-787-update.

[4] Fatt MSH, Lin C. Perforation of clamped, woven E-glass/polyester panels. Compos B Eng 2004;35(5):359–78.

[5] Walter TR, Subhash G, Sankar B, Yen C. Damage modes in 3D glass fiber epoxy woven composites under high rate of impact loading. Compos B Eng 2009;40(6):584–9.

[6] Meyers MA. Dynamic behavior of materials. New York: John Wiley & Sons; 1994.

[7] Abrate S. Impact of composite structures. New York: Cambridge University Press; 1998.

[8] Sikarwar R, Velmurugan R, Gupta NK. Influence of fiber orientation and thickness on the response of glass/epoxy composites subjected to impact loading. Compos B Eng 2014;60:627–36.

[9] Ahmadi H, Liaghat GH, Sabouri H, Bidkhouri E. Investigation on the high velocity

impact properties of glass-reinforced fiber metal laminates. J Compos Mater 2013;47(13):1605–15.

[10] Reddy RS, Reddy TS, Madhu V, Gogia AK, Rao KV. Behavior of E-glass composite laminates under ballistic impact. Mater Des 2015;84(5):79–86.

[11] Rolfe EKC, Quinn R, Hooper PA, Arora H, Dear JP. High velocity impact and blast loading of composite sandwich panels with novel carbon and glass construction. Journal of Dynamic Behavior of Materials 2018;4(3):359–72.

[12] Garcia-Castillo SK, Navarro C, Barbero E. Damage in preloaded glass/vinylester composite panels subjected to high-velocity impacts. Mech Res Commun 2014;55:66–71.

[13] Ansari MM, Chakrabarti A, Iqbal MA. An experimental and finite element investigation of the ballistic performance of laminated GFRP composite target. Compos B Eng 2017;125:211–26.

[14] Hoo Fatt MS, Lin C, Revilock DM, Hopkins DA. Ballistic impact of GLARE™ fiber–metal laminates. Compos Struct 2003;61(1–2):73–88.

[15] Bikakis GSE, Dimou CD, Sideridis EP. "Ballistic impact response of fiber–metal laminates and monolithic metal plates consisting of different aluminum alloys. Aero Sci Technol 2017;69:201–8.

[16] Domun N, Paton KR, Hadavinia H, Sainsbury T, Zhang T, Mohamud H. Enhancement of fracture toughness of epoxy nanocomposites by combining nanotubes and nanosheets as fillers. Materials 2017;10(10):1179.

[17] Ladani RB, Bashin M, Wu S, Ravindran AR, Ghorbani K, Zhang J, Kinloch AJ, et al. Fracture and fatigue behaviour of epoxy nanocomposites containing 1-D and 2-D nanoscale carbon fillers. Eng Fract Mech 2018. https://doi.org/10.1016/j.engfracmech.2018.04.033.

[18] Chatterjee S, Nafezarefi F, Tai NH, Schlagenhauf L, et al. Size and synergy effects of nanofiller hybrids including graphene nanoplatelets and carbon nanotubes in mechanical properties of epoxy composites. Carbon 2012;50:5380–6.

[19] Li W, Dichiara A, Bai J. Carbon nanotube–graphene nanoplatelet hybrids as high-performance multifunctional reinforcements in epoxy composites. Compos Sci Technol 2013;74:221–7.

[20] Yang S-Y, Lin W-N, Huang Y-L, Tien H-W, Wang J-Y, Ma C-C, Li S-M, Wang Y-S. Synergetic effects of graphene platelets and carbon nanotubes on the mechanical and thermal properties of epoxy composites. Carbon 2011;49(3):793–803.

[21] Johnsen B, Kinloch AJ, Mohammed RD, Taylor AC, Sprenger S. Toughening mecahnisms of nanoparticle-modified epoxy polymers. Polymer 2007;530–41.

[22] Tehrani M, Boroujeni AY, Hartman TB, Haugh TP, Case SW, Al-Haik MS. Mechanical characterization and impact damage assessment of a woven carbon fiber reinforced carbon nanotube-epoxy composite. Compos Sci Technol 2013;75:42–8.

[23] Laurenzi S, Pastore R, Giannini G, Marchetti M. Experimental study of impact resistance in multi-walled carbon nanotube reinforced epoxy. Compos Struct 2013;99:62–8.

[24] Rahman M, Hosur M, Zainuddin S, Vaidya U, Tauhid A, Kumar A. Effects of amino-functionalized MWCNTs on ballistic impact performance of E-glass/epoxy composites using a spherical projectile. Int J Impact Eng 2013;57:108–18.

[25] Naik NK, Pandya KS, Kavala VR, Zhang W, Koratkar NA. High-strain rate compressive behavior of multi-walled carbon nanotube dispersed thermoset epoxy resin. J Compos Mater 2015;49(8):903–10.

[26] Pandya KS, Naik NK. Analytical and experimental studies on ballistic impact behaviour of carbon nanotube dispersed resin. Int J Impact Eng 2015;76:49–59.

[27] Pol MH, Liaghat G, Zamani E, Ordys A. Investigation of the ballistic impact behavior of 2D woven glass/epoxy/nanoclay nanocomposites. J Compos Mater 2014;49(12):1449–60.

[28] Pol M, Liaghat GH, Hajiarazi F. Effect of nanoclay on ballistic behavior of woven fabric composites: experimental investigation. J Compos Mater 2012;47(13):1563–73.

[29] Avila A, Neto A, Nascimento Jr. H. Hybrid nanocomposites for mid-range ballistic protection. Int J Impact Eng 2011;38:669–75.

[30] Domun N, Hadavinia H, Zhang T, Liaghat GH, Vahid S, Paton K, Spacie C, Sainsbury T. Improving the fracture toughness properties of epoxy using graphene nanoplatelets at low filler content. Nanocomposites 2017;3(3):85–96.

[31] Kaboglu C, Mohagheghian I, Zhou J, Guan Z, Cantwell W, John S, Blackman BRK, Kinloch AJ, Dear JP. High-velocity impact deformation and perforation of fibre metal laminates. J Mater Sci 2018;53(6):4209–28.

[32] " ARAMIS user manual – software v6.3," ARAMIS. Braunschweig Germany: GOM mBH; 2011.

[33] Rajan V, Rossol M, Zok F. Optimization of digital image correlation for high-resolution strain mapping of ceramic composites. Exp Mech 2012;52(9):1407–21.

[34] Zhou X, Shin E, Wang KW, Bakis CE. Interfacial damping characteristics of carbon nanotube-based composites. Compos Sci Technol 2004;64(15):2425–37.

[35] Buldum A, Jian PL. Atomic scale sliding and rolling of carbon nanotubes. Phys Rev Lett 1999;83(24):5050–3.

[36] Liu B, Zhang H, Fernandes H, Maldague X. Quantitative evaluation of pulsed thermography, lock-in thermography and vibrothermography on foreign object defect (FOD) in CFRP. Sensors 2016;16:743.

[37] Thermal wave imaging [online]. Available:. https://www.thermalwave.com/1/376/mosaiq.asp, Accessed date: 4 September 2018.

[38] Kidd G, Nunn J. Application of pulsed thermography to quality assurance of thermal barrier coatings. Proc. IMechE Part G: J Aerosp Eng 2011;226:873–80.

[39] Sun J. Analysis of data processing methods for pulsed thermal imaging characterisation of delaminations. Quantitative InfraRed Thermography Journal 2013;10:9–25.

[40] Maldague XP. Theory and practice of infrared technology for non-destructive testing. New York: John Wiley Interscience; 2001.

[41] Czichos H. Handbook of technical diagnostics. Berlin/Heidelberg: Springer Verlag; 2013. Germany.

[42] Zeng Z, Tao N, Feng LC, Li YS, Zhang CL. Relative thermal contrast analysis in the inspection of wind turbine blades using pulsed thermography. Adv Mater Res 2011;301–303:591–6.

[43] Wróbel G, Pawlak S, Muzia G. Thermal diffusivity measurements of selected fiber reinforced polymer composites using heat pulse method. Archives of Materials Science and Engineering 2011;48(1):25–32.